Objectively mapping HF radar-derived surface current data using measured and idealized data covariance matrices

Sung Yong Kim,[1] Eric Terrill,[1] and Bruce Cornuelle[2]

Received 16 May 2006; revised 7 February 2007; accepted 22 March 2007; published 26 June 2007.

[1] Surface currents measured by high-frequency radars are objectively mapped using covariance matrices computed from hourly surface current vectors spanning two years. Since retrievals of surface radial velocities are inherently gappy in space and time, the irregular density of surface current data leads to negative eigenvalues in the sample covariance matrix. The number and the magnitude of the negative eigenvalues depend on the degree of data continuity used in the matrix computation. In a region of 90% data coverage, the negative eigenvalues of the sample covariance matrix are small enough to be removed by adding a noise term to the diagonal of the matrix. The mapping is extended to regions of poorer data coverage by applying a smoothed covariance matrix obtained by spatially averaging the sample covariance matrix. This approach estimates a stable covariance matrix of surface currents for regions with the intermittent radar coverage. An additional benefit is the removal of baseline errors that often exist between two radar sites. The covariance matrices and the correlation functions of the surface currents are exponential in space rather than Gaussian, as is often assumed in the objective mapping of oceanographic data sets. Patterns in the decorrelation length scale provide the variabilities of surface currents and the insights on the influence of topographic features (bathymetry and headlands). The objective mapping approach presented herein lends itself to various applications, including the Lagrangian transport estimates, dynamic analysis through divergence and vorticity of current vectors, and statistical models of surface currents.

Citation: Kim, S. Y., E. Terrill, and B. Cornuelle (2007), Objectively mapping HF radar-derived surface current data using measured and idealized data covariance matrices, *J. Geophys. Res.*, *112*, C06021, doi:10.1029/2006JC003756.

1. Introduction

[2] The surface current measurement by interpretation of radio waves (3–30 MHz) backscattered from surface gravity waves is quickly maturing as an oceanographic observational tool whose data is useful to a broad range of users. The shore-based antenna approach can provide continuous temporal and broad spatial surface current observations, facilitating the delivery of data in near real-time for various applications.

[3] The complicated signal processing for extracting surface currents from the backscattered radar signals [*de Paolo and Terrill*, 2007] yields radial velocities on polar coordinate grid points centered by each antenna location. Radial velocities measured by multiple antenna installations have been combined into current vector field using the unweighted least squares fitting [*Lipa and Barrick*, 1983] (M. Cook's HFRadarmapVer4.1 MATLAB toolbox). The maps of ocean surface currents are gappy in space and time for three reasons. First, the MUSIC algorithm on the measured Doppler spectrum does not provide a solution for all bearing angles. Second, the estimate of current vectors along the baseline between two radars where the measurements of radial velocities are nearly aligned suffers from poor geometrical dilution of precision (GDOP), and frequently results in spurious current vectors. The region with radial velocities crossing at angles less than 15–20 degrees between two radars is commonly considered to produce unusable current vectors. Finally, hardware or software problems can lead to the temporary shutdown of individual radar sites.

[4] Relevant applications of surface currents require time- and space-continuous data, which requires the interpolation of the gappy observations to a regularly spaced product. A popular approach involves projecting the observations on the dominant modes of the sample covariance matrix (EOFs) [*Boyd et al.*, 1994; *Beckers and Rixen*, 2003; *Alvera-Azcarate et al.*, 2005; *Houseago-Stokes and Challenor*, 2004]. The anomalies of the missing data are estimated iteratively, and the optimal number of EOFs and the number of iterations are determined by cross validation with randomly selected observations and their estimates. Since the data set of surface currents measured by high-frequency (HF) radars around San Diego is not prefil-

[1]Marine Physical Laboratory, Scripps Institution of Oceanography, La Jolla, California, USA.
[2]Physical Oceanography Research Division, Scripps Institution of Oceanography, La Jolla, California, USA.

0148-0227/07/2006JC003756$09.00

tered and includes errors and uncertainties due to radar operations [*Graber et al.*, 1997], the first few EOFs may not explain the variability of observed surface currents effectively without elaborate quality control before computing the covariance matrix.

[5] Another approach used with geophysical data is the expectation maximization (EM) method, which estimates the anomalies of the missing data with iteration using an error covariance matrix as the regularization matrix [*Orchard and Woodbury*, 1972; *Schneider*, 2001; *Beckenbach and Washburn*, 2004]. The covariance matrix is estimated with the demeaned missing data substituted by zeros at the first iteration in order to avoid non-positive definiteness, and is updated with estimated missing data until convergence. Since the EM method estimates only missing data, the estimated covariance matrix may be discontinuous with nearby points.

[6] Several approaches have been proposed for interpolation, such as normal mode analysis [*Lipphardt et al.*, 2000], and objective analysis [*Bretherton et al.*, 1976; *Denman and Freeland*, 1985; *Hollingsworth and Lönnberg*, 1986; *Brankart and Brasseur*, 1996]. These methods are all closely related. In particular, objective analysis can be implemented as normal mode analysis or EOF analysis [*Davis*, 1985].

[7] In this paper, an objective mapping method is presented that applies the sample covariance matrix computed directly from observations of hourly averaged surface current vectors during two year. This approach, although computationally cumbersome, is now technically feasible due to advances in computing power. It has a number of advantages, including: the covariance matrix is based directly on the observations, with no intermediate interpolation step; the calculation of the matrix is fast and simple, without iteration; and the method can include both time and space covariances. The main disadvantage of this method is the sensitivity to negative eigenvalues in the sample covariance matrix, which can arise from missing data. The negative eigenvalues can be mitigated by adding a noise term to the diagonal of the sample covariance matrix, effectively attenuating the components with negative eigenvalues. The EOF reconstruction approach was also tried, but needed to be severely limited in space because of outliers in the current vectors.

[8] The analysis in this paper contains in the three sections. In section 2, the outlier removal as a primitive data quality control process is described, and basic statistics of the surface currents are presented. The statistics are the standard deviation, the power spectrum, and the spatial structure of correlations. Section 3 contains the gridding using the sample and smoothed covariance matrices and the regularization and the estimation of decorrelation scales of surface current. The approach used to estimate a smoothed homogeneous two-dimensional data covariance matrix from the four-dimensional sample data-data covariance matrix is the focus of section 3.4. In section 4, the decorrelation length scales across the coast (section 4.1) and the uncertainty of objectively mapped currents (section 4.2) are discussed. Examples of time series and vector fields of gridded surface currents are presented (section 4.4). In this paper, u and v denote the eastward component and the northward component of the surface current. There is no rotation of coordinate system; the x and y directions correspond to east and north, respectively.

2. Observations

2.1. Coverage

[9] An array of high-frequency (about 25 MHz) direction-finding-style system for the measurement of surface currents (Codar Ocean Sensors, Palo Alto, CA) has been deployed in the San Diego region since September 2002. Individual radar sites are located at Point Loma (SDPL), Border Field State Park on the U.S.-Mexico Border (SDBP), and an offshore station at the Coronado Islands (SDCI) (Figure 1).

[10] The fractional availability of surface current vectors at each grid point during two years duration (April 2003–March 2005) is shown in Figure 2a. The existence of current vector solutions depends strongly on the number and bearing angle diversity of the radial velocities within a search range of each grid point. Since at least two radial velocities from different sites are required for a vector solution, the regions with overlapping radar range cells from multiple sites show better coverage through time.

[11] The timeline of available radial velocities at each radar site is shown in Figure 3a. The surface current vectors derived from radial velocities using measured beam patterns at three sites (SDPL, SDBP, and SDCI) are used for the analysis in this paper. Figure 3b shows the percentage coverage relative to the grid points shown in Figure 1 through time. The temporary disruption of a single radar unit in a sparse array of radar units will reduce the coverage of total vector solutions.

[12] The physical overview of surface currents is restricted to grid points with at least 45% current vector availability during the two year period, as indicated in Figure 1. The estimation of the data-data covariance matrix is limited to the domain of at least 90% coverage. Covariance matrices computed from regions with many missing data have unacceptably large negative eigenvalues, and will be presented in section 4.2 and Figure 10.

2.2. Outlier Removal

[13] The outliers in the vector surface current data lie in the tail of its probability density function. The identification of outliers follows as described below. A 2-day running mean of the time series, which is consistent with the duration of the local ocean's response to wind events, is subtracted to produce a high-pass filtered time series. The anomaly time series are then passed through a moving 5-day window in which the deviation from the 5-day running mean is compared to the 5-day running standard deviation. The hourly data during 5 days provide enough realizations for the detection of statistically anomalous data. Anomalies outside five standard deviations from the 5-day running mean are flagged as outliers. Figure 2b shows the percentage of identified outliers during two years. Outliers are typically clustered on the baseline and at the edges of radar coverage regions. Although most outliers are flagged in this process, a significant number remain behind.

[14] The baseline, defined as the line of sight between two radars, is the place where it is difficult to resolve vector solutions from nearly parallel radial velocities which weakly

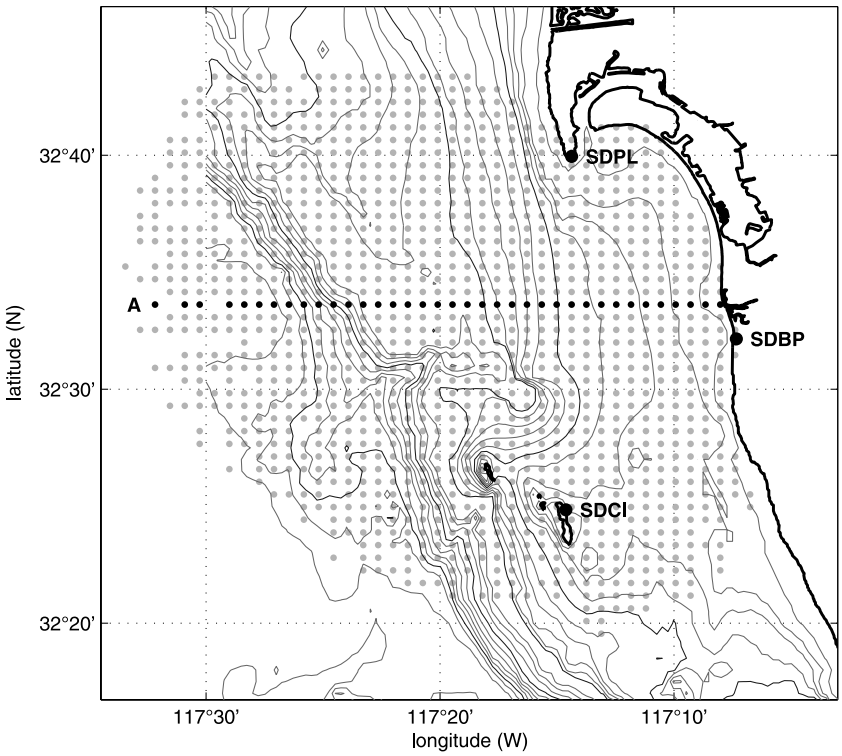

Figure 1. The dotted area is the observation domain of surface currents measured by high-frequency radars in San Diego with temporal coverage of 45% or more (during the time span of April 2003–March 2005). The high-frequency radar sites are SDPL (Point Loma), SDBP (Border Field State Park), and SDCI (Coronado Islands). Grid line A denotes the reference axis of decorrelation length scale in Figure 9. The bottom bathymetry contours are indicated by the thin lines with 10 m ($0 < z < 100$ m) and 100 m ($100 < z < 1000$ m) contour intervals and the thick lines at the 50, 100, 500, and 1000 m contours.

constrain the current vector normal to the baseline. Vector solutions using the standard unweighted least squares fit can be spurious, which should be identified as outliers. The baseline has also higher GDOP, which is determined by both the number of available radial velocities within the search range of a vector grid point and their location relative to the radar [*Lipa and Barrick*, 1983; *Gurgel*, 1994; *Chapman, et al.*, 1997; *Levanon*, 2000].

[15] The procedure for the preparation of the data set is to interpolate radial velocities across a radar range cell if the

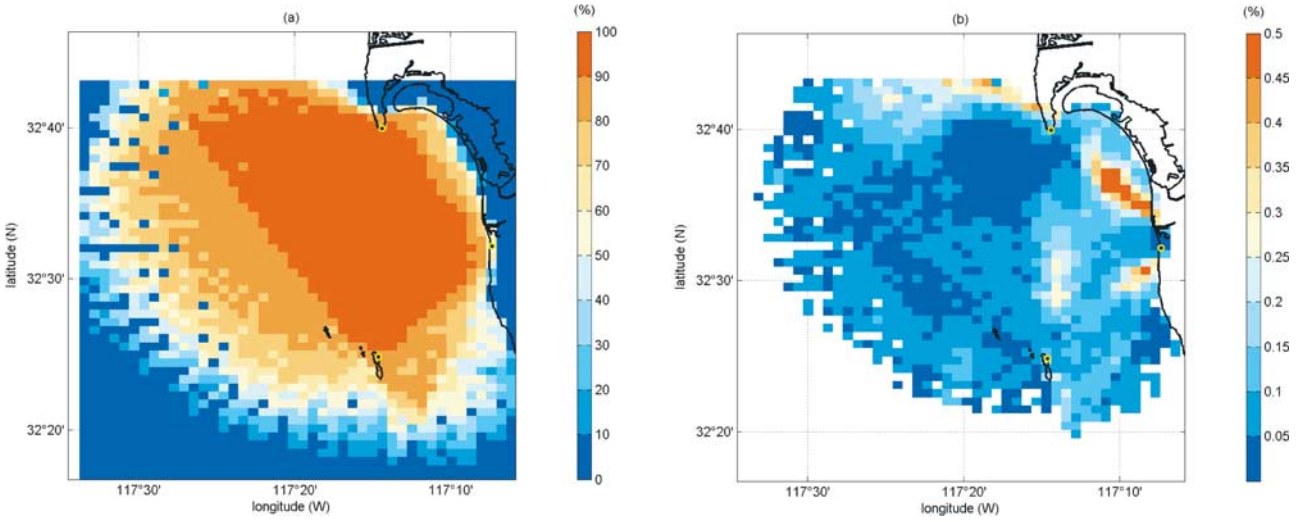

Figure 2. (a) A map of temporal data coverage at all grid points. (b) The percentage of observations identified as outliers during two years of operation (April 2003–March 2005).

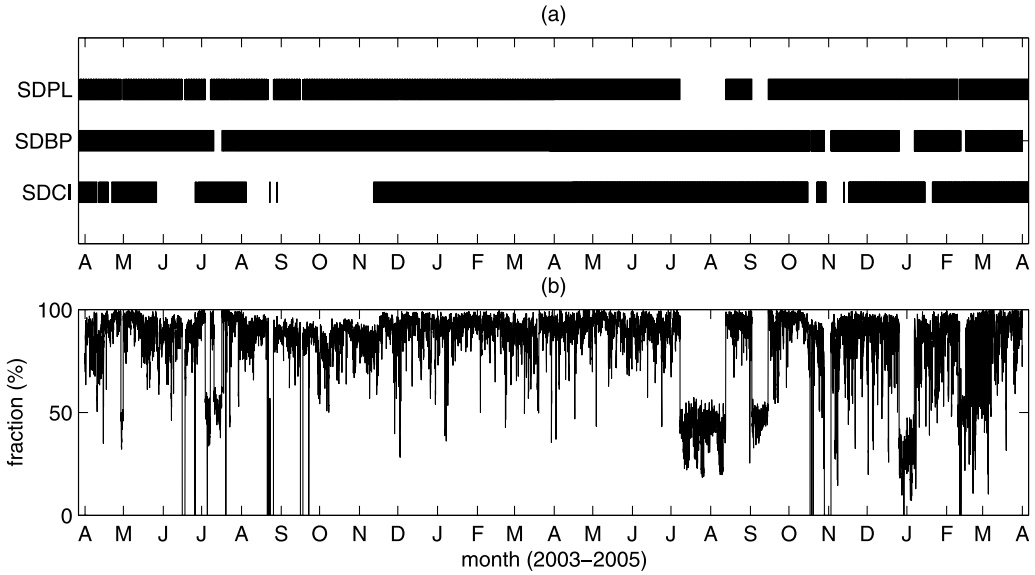

Figure 3. (a) The timeline of available radial velocities at each radar site. (b) The time series of percentage coverage relative to 45% coverage area.

radial velocities are missing within 15 degrees prior to vector combination, and to remove the outliers among the combined current vectors using the approach described above. There are no other QA/QC processes beyond these two steps.

2.3. Basic Statistics

[16] Southeastward flowing surface currents are typical south of San Diego, as shown in Figure 4a. In general, the surface currents pass south of Point Loma and bend into the embayment created by the headland, with flow complications arising from San Diego Bay outflow, local gradients in wind forcing, and eddies. The offshore currents are stronger than near-shore currents and are nearly unidirectional. The offshore is defined herein as the area farther than 30 km from the coast, and near-shore is the region within 30 km of the coast. During the analysis of the multi-year data set, the long term temporal mean (not shown) was found to exhibit a local artifact in a sector at approximately 287 degrees from true north at the SDBP site. Further investigation revealed that this artifact resulted from an anomaly in the measured beam pattern of the SDBP site, which showed a bias in radial solutions across a 5 degree wide angular bin. While the bias is visible in Figure 4b, Figure 6c, and the temporal mean

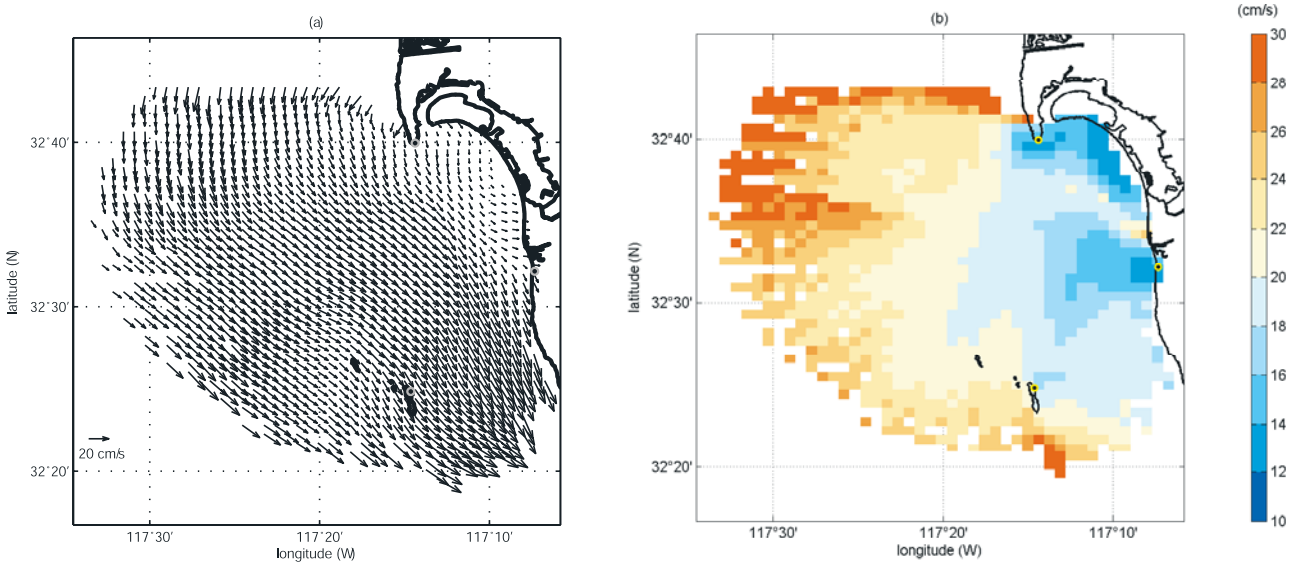

Figure 4. (a) A typical example of surface current vectors around San Diego. (b) The standard deviation of surface current magnitudes. Higher standard deviations along the baseline (SDPL-SDBP) result from the poor geometrical dilution of precision.

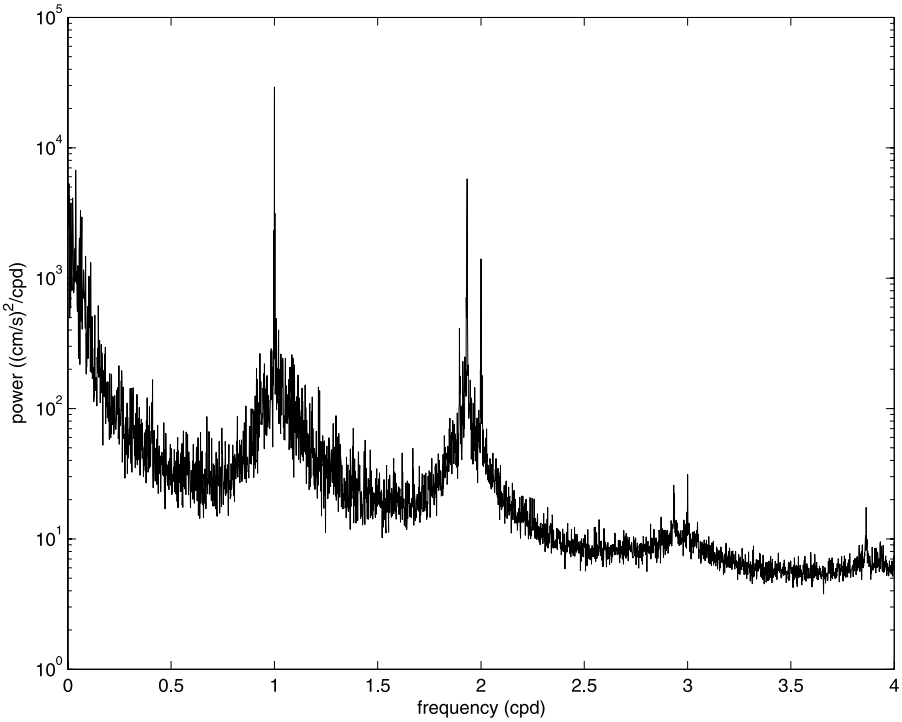

Figure 5. The frequency-bin-averaged power spectrum of hourly surface current vectors in the region with 90% or greater coverage (510 grid points) shows that the dominant variances are at the low frequencies (less than 0.4 cpd), and the main tidal frequencies (K1, S1, and M2) and their harmonics.

currents as discontinuous features in this sector, it affects less than 8% of grid points. Since the smoothed covariance matrix and its decorrelation length scales presented herein are estimated from the spatial average of the sample data covariance matrix, the artifact has a minimal impact on this analysis.

[17] The standard deviation of the surface current magnitudes is shown in Figure 4b. The standard deviations along the baselines are significantly larger than elsewhere due to the tendency of the baseline to generate spurious results. In this paper, the standard deviation at the baseline between SDPL and SDBP shows some high values even after removal of outliers. The standard deviations of off-shore currents are generally larger than near-shore currents, which may also be partly traceable to the inversion from radials.

[18] The frequency-bin-averaged power spectrum of the surface current vectors averaged over all grid points with at least 45% temporal coverage (Figure 1) is shown as Figure 5. Clear peaks of variance are at the low frequency band, defined herein as frequencies less than 0.4 cycle per day (cpd), the main tidal frequencies (S1, K1 and M2) and their harmonics. The spreading of the energy around the tidal peaks is partly due to nonlinear interactions with the low-frequency flow [*Munk and Cartwright*, 1966; *Essen et al.*, 1983].

[19] The correlation coefficients (equation (3)) between surface currents at different grid points show the statistical spatial structure of surface currents such as the decorrelation length scale and the shape of the correlation function. The decorrelation length scale characterizes the typical scales of variability, and the correlation can identify inconsistent or abrupt features in the spatial domain and detect bad points.

[20] The correlations of eastward currents, $\rho_{uu}(\mathbf{x}, \mathbf{x}')$, between a reference grid point ($\mathbf{x}$) and all other grid points ($\mathbf{x}'$) are shown in Figure 6. In the same way, the correlations of northward currents, $\rho_{vv}(\mathbf{x}, \mathbf{x}')$, are shown in Figure 7. Examples of the correlations are shown for two off-shore grid points (Figures 6a, 6c, 7a and 7c) and two near-shore points (Figures 6b, 6d, 7b and 7d). The correlations at the offshore reference points show larger highly correlated areas compared with the near-shore points. The north-south flows have more directional preferences in their correlations than the east-west flows. The cross-correlations, $\rho_{uv}(\mathbf{x}, \mathbf{x}')$ and $\rho_{vu}(\mathbf{x}, \mathbf{x}')$, have complicated structures in space and vary within ±0.3, which is not much above the level of no significance.

[21] The cross sections of correlation in latitude (Figures 8a and 8b) and in longitude (Figures 8c and 8d) are shown for eastward currents (u) and northward currents (v), respectively. These cross sections are aligned to have a common origin and appear more exponential than Gaussian. The discontinuous lines result from data gaps within 45% coverage region (top of Figure 8) and the Coronado Islands (bottom of Figure 8).

[22] Although the individual correlation functions of surface currents driven by a simple forcing such as wind, tides (diurnal and semidiurnal), and the low frequency pressure gradient (Figure 5) are different, we do not decompose the surface currents before mapping. Band-passing gappy data to isolate different physics adds significant complexity to the procedure. Analysis has shown that the band-passed

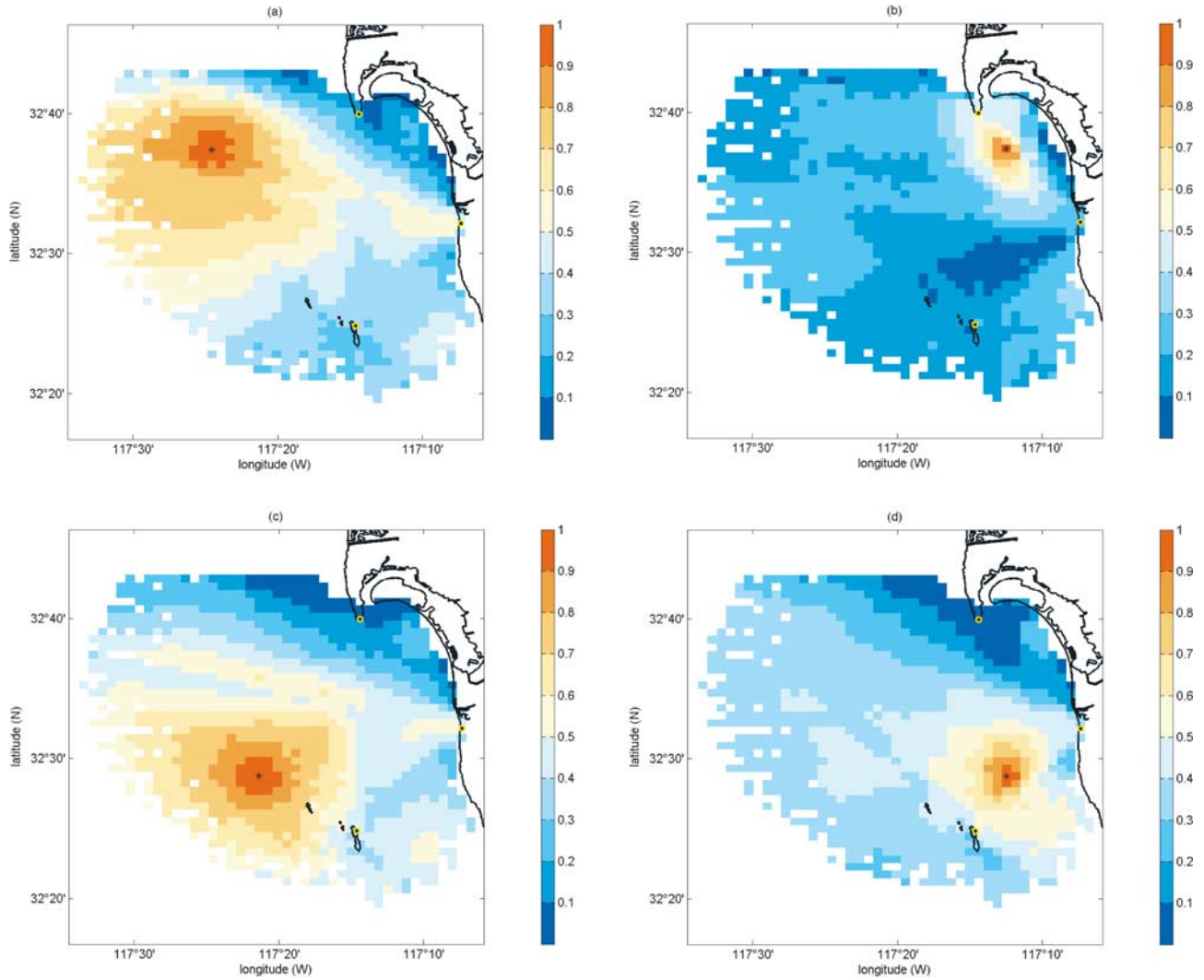

Figure 6. The correlations of eastward currents, $\rho_{uu}(\mathbf{x}, \mathbf{x}')$, between a reference point, $\mathbf{x}$, and all other grid points, $\mathbf{x}'$. The four reference points are (a) offshore point A (32° 37.40′N 117° 24.55′W), (b) nearshore point B (32° 37.40′N 117° 12.47′W), (c) offshore point C (32° 28.75′N 117° 21.37′W), and (d) nearshore point D (32° 28.75′N 117° 12.47′W).

correlation functions all have exponential shape but different decorrelation length scales. The sample data covariance matrices is the sum of the covariance matrix of all components.

3. Methods

3.1. Data Covariance

[23] The sample data covariance matrix, $\mathbf{C}(\mathbf{x}, \mathbf{x}')$, with zero time lag is written as

$$\mathbf{C}(\mathbf{x}, \mathbf{x}') = \frac{1}{\mathbf{N}(\mathbf{x}, \mathbf{x}')} \sum_{t \epsilon (\mathbf{x} \cap \mathbf{x}')} \mathbf{u}(\mathbf{x}, t)\mathbf{u}^{\mathrm{T}}(\mathbf{x}', t), \tag{1}$$

where $\mathbf{u}(\mathbf{x}, t) = [u(\mathbf{x}, t)\ v(\mathbf{x}, t)]^{\mathrm{T}}$ denotes the concatenated current vector observations, which have $2M \times L$ (for 90% coverage during two year time span, there are 510 grid points, so $2M = 1020$, $L = 17544$) elements. M and L are the number of grid points and time points, respectively. $\mathbf{N}(\mathbf{x}, \mathbf{x}')$ is the number of time with observations at both $\mathbf{x}$ and $\mathbf{x}'$, and is less than L due to missing data.

[24] The observed data covariance matrix, $\mathbf{C}(\mathbf{x}, \mathbf{x}')$, is the sum of the true covariance matrix, $\mathbf{C}_t(\mathbf{x}, \mathbf{x}')$, and the error covariance, $\mathbf{Q}(\mathbf{x}, \mathbf{x}')$, which includes the observation errors due to measurement noise and the statistical errors due to missing data and finite averaging time.

$$\mathbf{C}(\mathbf{x}, \mathbf{x}') = \mathbf{C}_t(\mathbf{x}, \mathbf{x}') + \mathbf{Q}(\mathbf{x}, \mathbf{x}') \tag{2}$$

3.2. Correlation Coefficients

[25] The correlation coefficient, $\rho(\mathbf{x}, \mathbf{x}')$, between any two grid points is,

$$\rho(\mathbf{x}, \mathbf{x}') = \begin{bmatrix} \frac{1}{\sigma_u(\mathbf{x})} & 0 \\ 0 & \frac{1}{\sigma_v(\mathbf{x})} \end{bmatrix} \mathbf{C}(\mathbf{x}, \mathbf{x}') \begin{bmatrix} \frac{1}{\sigma_u(\mathbf{x}')} & 0 \\ 0 & \frac{1}{\sigma_v(\mathbf{x}')} \end{bmatrix} = \begin{bmatrix} \rho_{uu} & \rho_{uv} \\ \rho_{vu} & \rho_{vv} \end{bmatrix}, \tag{3}$$

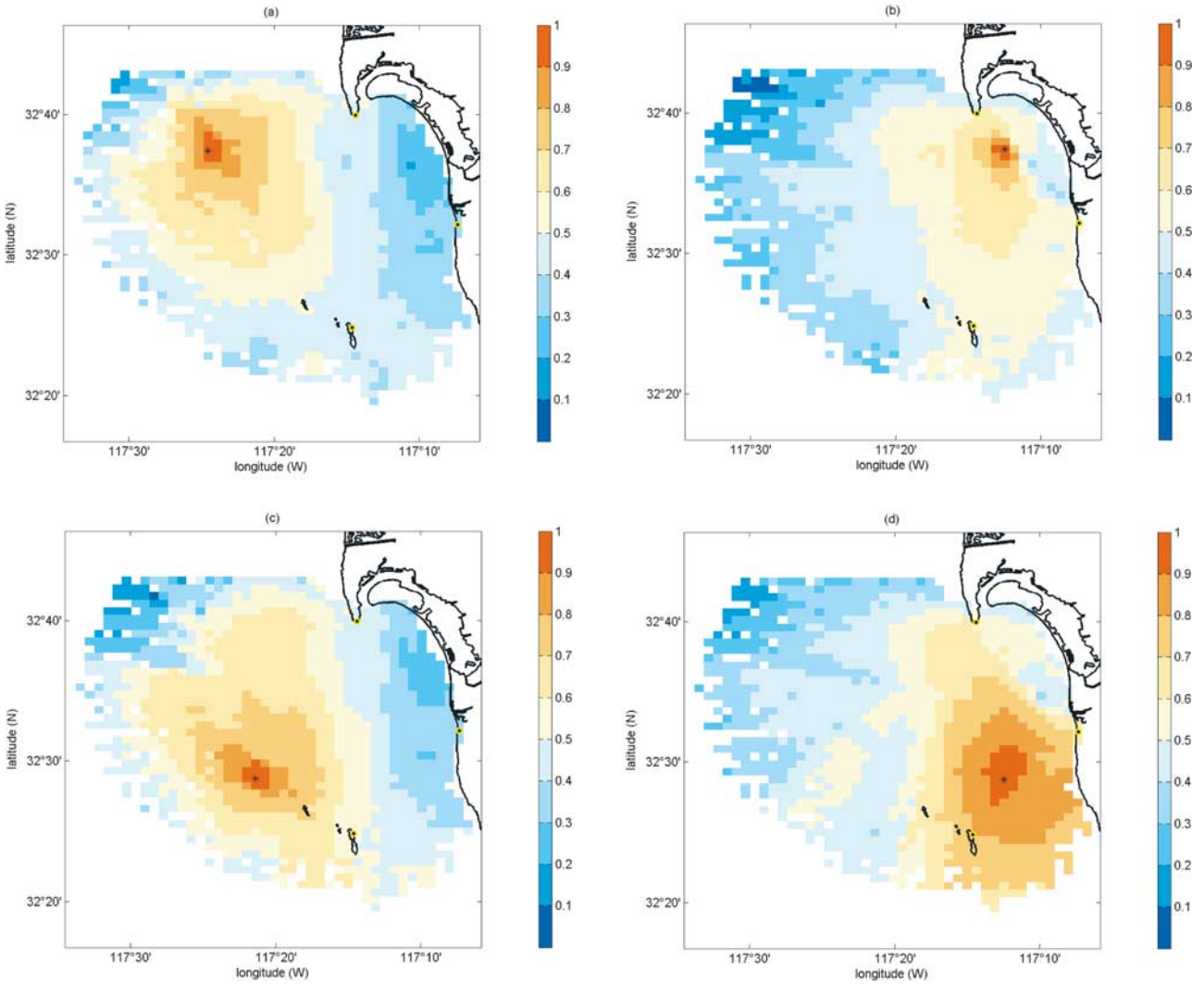

Figure 7. The correlations of northward currents, $\rho_{vv}(\mathbf{x}, \mathbf{x}')$, between a reference point, $\mathbf{x}$, and all other grid points, $\mathbf{x}'$. The four reference points are (a) offshore point A (32° 37.40′N 117 24°.55′W), (b) nearshore point B (32° 37.40′N 117° 12.47′W), (c) offshore point C (32° 28.75′N 117° 21.37′W), and (d) nearshore point D (32° 28.75′N 117° 12.47′W).

where $\sigma(\mathbf{x}) = [\sigma_u(\mathbf{x})\ \sigma_v(\mathbf{x})]^{\mathrm{T}}$ is the time-averaged standard deviation of $u(\mathbf{x}, t)$ and $v(\mathbf{x}, t)$, respectively.

3.3. Gridding Using Sample Data Covariance Matrix

[26] Since the sample data covariance matrix is calculated by the anomalies from the time mean of a given time span, the mapping of anomalies is considered.

$$\tilde{\mathbf{d}} = (\mathrm{cov}_{\mathrm{dm}})^{\mathrm{T}}(\mathrm{cov}_{\mathrm{dd}})^{-1}\mathbf{d}, \tag{4}$$

where $\mathrm{cov}_{\mathrm{dm}}(\mathbf{x}, \mathbf{x}')$ denotes the sample data-model covariance matrix, $\mathrm{cov}_{\mathrm{dd}}(\mathbf{x}, \mathbf{x}')$ the sample data-data covariance matrix, $\mathbf{d}$ the observed demeaned current vectors, and $\tilde{\mathbf{d}}$ is the estimated demeaned current vectors. The mapping grid coincides with the observation, so the two covariance matrices are the same, except that the data-model covariance matrix does not include the observational error. An observational error covariance matrix ($\mathbf{R}$), is added to the sample data covariance matrix which already includes error due to the finite and gappy sampling.

$$\mathrm{cov}_{\mathrm{dm}}(\mathbf{x}, \mathbf{x}') = \mathbf{C}(\mathbf{x}, \mathbf{x}') \tag{5}$$

$$\mathrm{cov}_{\mathrm{dd}}(\mathbf{x}, \mathbf{x}') = \mathbf{C}(\mathbf{x}, \mathbf{x}') + \mathbf{R} \tag{6}$$

[27] In the mapping using the sample covariance matrix ($\mathbf{C}$), the regularization matrix ($\mathbf{R}$) is usually defined by the noise level of the observed data relative to the current variance (e.g., the intrinsic uncertainty of instruments). Since the sample covariance matrix is not positive definite due to missing data, the regularization matrix makes the data-data covariance matrix ($\mathrm{cov}_{\mathrm{dd}}$) invertible. It is assumed that the regularization matrix is a scaled identity matrix.

$$\mathbf{R} = \gamma^2\mathbf{I}, \tag{7}$$

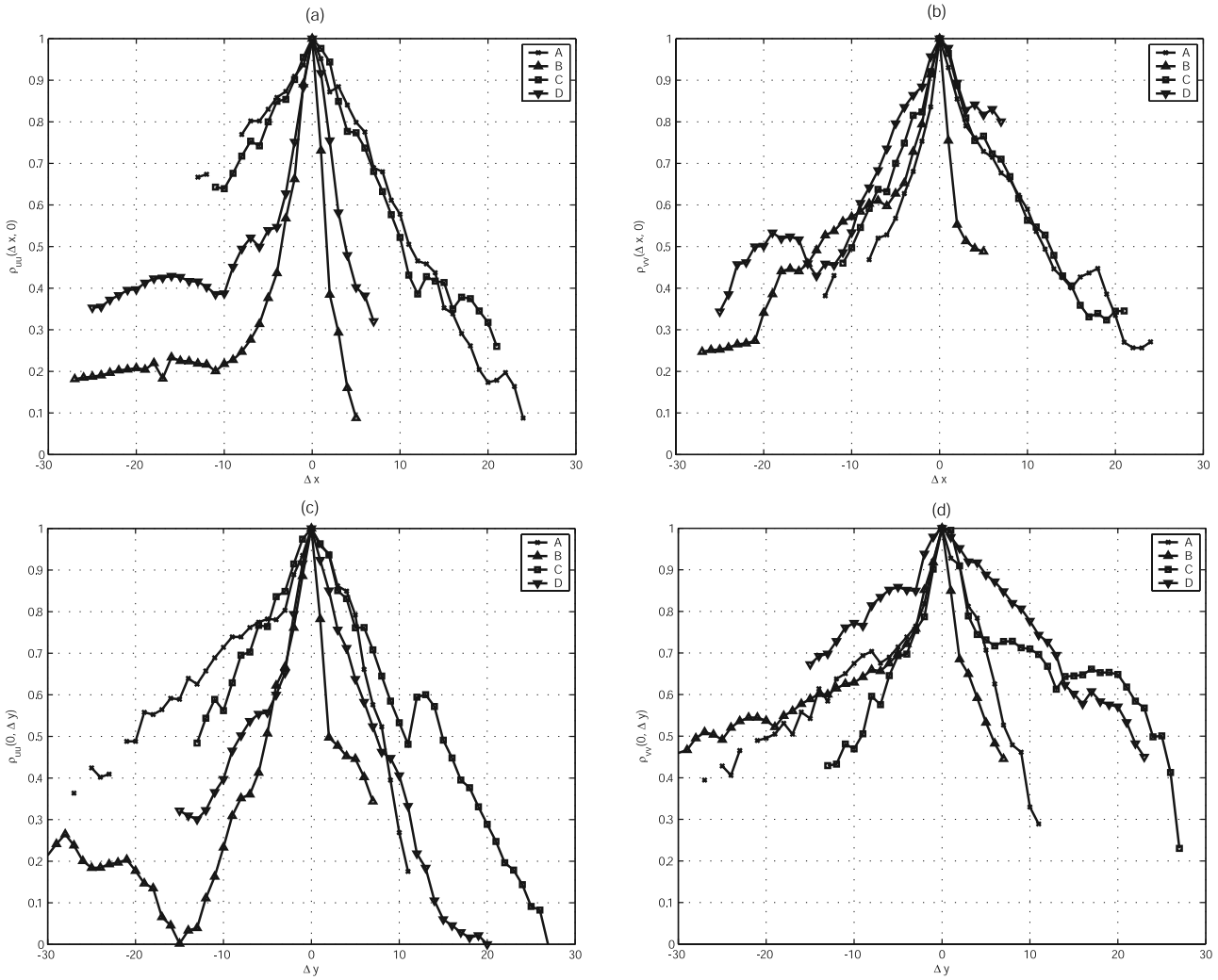

Figure 8. Latitudinal and longitudinal cross sections of two-dimensional correlations aligned to have a common origin on the Δx axis (or Δy axis): (a) $\rho_{uu}(\Delta x)$, (b) $\rho_{vv}(\Delta x)$, (c) $\rho_{uu}(\Delta y)$, and (d) $\rho_{vv}(\Delta y)$.

The mean eigenvalue (γ^2) of the regularization matrix should be greater than the magnitude of the smallest negative eigenvalue of the sample covariance matrix (equation (10)), which is decomposed into orthogonal eigenvectors ($\mathbf{p}_k$) and eigenvalues (λ_k).

$$\mathbf{C}(\mathbf{x}, \mathbf{x}') = \sum_k \mathbf{p}_k \lambda_k \mathbf{p}_k^{\mathrm{T}} \tag{8}$$

The mapping matrix is approximated schematically by,

$$\mathrm{cov}_{\mathrm{dm}}^{\mathrm{T}} \mathrm{cov}_{\mathrm{dd}}^{-1} = \sum_k \mathbf{p}_k \left(\frac{|\lambda_k|}{|\lambda_k| + \gamma^2} \right) \mathbf{p}_k^{\mathrm{T}}, \tag{9}$$

where $\mathbf{p}_k^{\mathrm{T}} \mathbf{p}_k = \mathbf{p}_k \mathbf{p}_k^{\mathrm{T}} = \mathbf{I}$ ($k = 1,2,\ldots,2M$) (equation (9) is valid only when all observations are present).

$$|\min(\lambda_k)| < \gamma^2 \tag{10}$$

The substitution of positive for negative eigenvalues in equation (9) does not change the covariance matrix by a significant amount compared to the statistical uncertainty in the 90% coverage regions. Maps using the covariance matrix without changing the sign of the eigenvalues are similar to those using equation (9). However, the simple sign change is not a general solution, because, for example, the variance becomes larger than in the sample covariance matrix.

3.4. Decorrelation Length Scale

[28] The composite averaged correlation coefficients, $\tilde{\rho}$ ($\mathbf{x}$, $\Delta\mathbf{x}$), are the spatial average of the correlations at the local grid points ($\hat{\mathbf{x}}$) within r_0 radius from a reference grid point ($\mathbf{x}$), and are fitted with the exponential function, $f(\Delta\mathbf{x})$.

$$\tilde{\rho}(\mathbf{x}, \Delta\mathbf{x}) = \frac{\sum_{\forall \hat{\mathbf{x}}} \mathbf{N}(\hat{\mathbf{x}}, \hat{\mathbf{x}} + \Delta\mathbf{x}) \rho(\hat{\mathbf{x}}, \hat{\mathbf{x}} + \Delta\mathbf{x})}{\sum_{\forall \hat{\mathbf{x}}} \mathbf{N}(\hat{\mathbf{x}}, \hat{\mathbf{x}} + \Delta\mathbf{x})}, \tag{11}$$

$$f(\Delta\mathbf{x}) = \exp\left[-\left\{ a(\Delta x)^2 + b(\Delta x)(\Delta y) + c(\Delta y)^2 \right\}^{\frac{1}{2}} \right]. \tag{12}$$

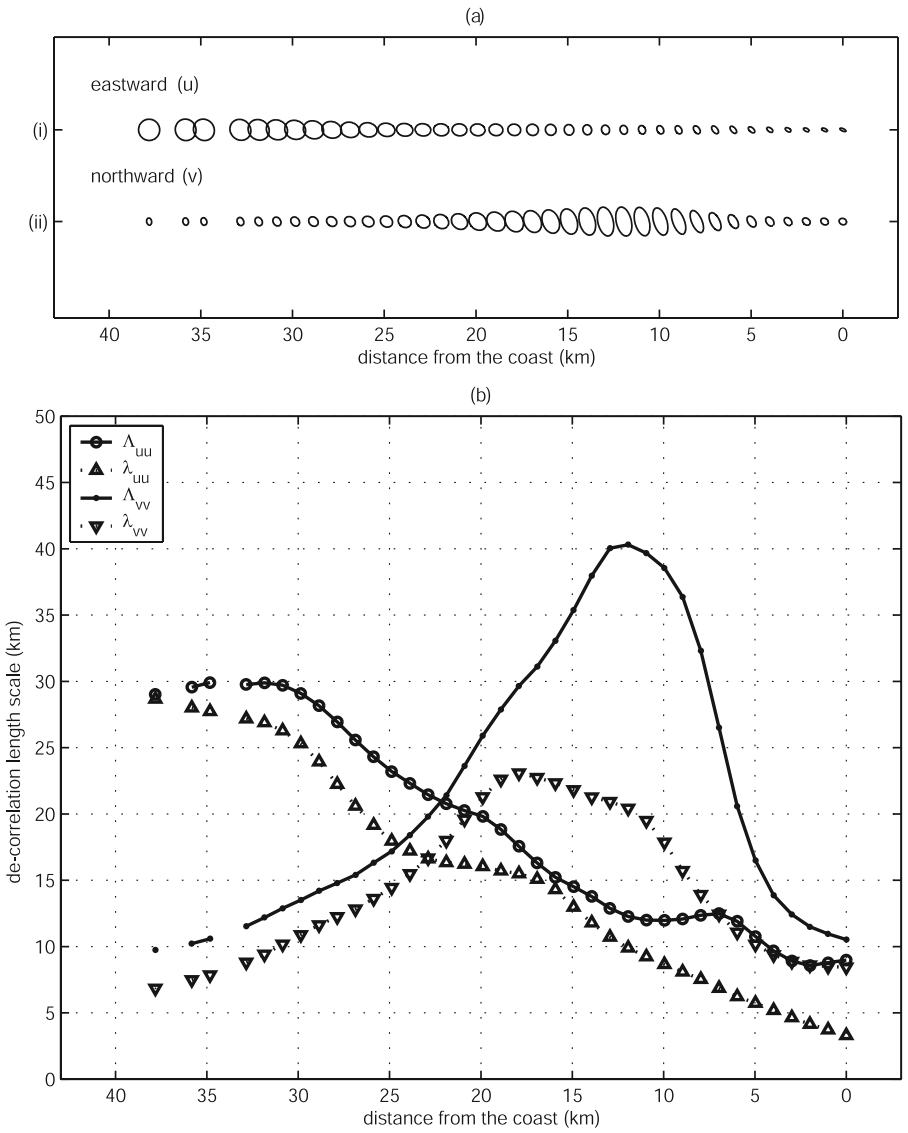

Figure 9. Decorrelation length scales of surface currents along grid line A in Figure 1. (a) Ellipses of (i) the east-west flow and (ii) the north-south flow. (b) Decorrelation length scales of near-coast surface currents (Λ and λ denote the semimajor and semiminor axes).

The composite averaged correlation for eastward currents (u) and northward currents (v) are calculated only within $\pm n\Delta x$ and $\pm n\Delta y$ from the center, because the signal-to-noise-ratio drops for larger lags. The coefficients (a, b, and c) are directly determined from minimizing the residual, $e(\mathbf{x})$, between $\tilde{\rho}(\mathbf{x}, \Delta\mathbf{x})$ and $f(\Delta\mathbf{x})$ with a given n.

$$e(\mathbf{x}) = \frac{1}{(2n+1)^2} \sum_{i=1}^{(2n+1)^2} \left[\tilde{\rho}(\mathbf{x}, \Delta\mathbf{x}_i) - f(\Delta\mathbf{x}_i)\right]^2 \qquad (13)$$

These coefficients can be converted to principal axes by

$$\lambda_x = \left(a\cos^2\theta - b\cos\theta\sin\theta + c\sin^2\theta\right)^{-\frac{1}{2}}$$

$$\lambda_y = \left(a\sin^2\theta + b\cos\theta\sin\theta + c\cos^2\theta\right)^{-\frac{1}{2}} \qquad (14)$$

$$\theta = \tfrac{1}{2}\arctan\tfrac{b}{c-a}$$

$$\Lambda = \max\left(\lambda_x, \lambda_y\right), \lambda = \min\left(\lambda_x, \lambda_y\right), \qquad (15)$$

where Λ and λ are the semimajor and semiminor axis, respectively, of the ellipse with the rotation angle (θ, positive clockwise) of the semimajor axis. The number of lags (n) is determined from stabilizing the decorrelation length scale, and is addressed with an example in section 4.1.

3.5. Homogeneous Covariance

[29] The sample mean correlation coefficient, $\bar{\rho}(\Delta\mathbf{x})$, is the average of correlation coefficients compositing the spatial lag ($\Delta\mathbf{x}$) across all grid points.

$$\bar{\rho}(\Delta\mathbf{x}) = \frac{\sum_{\forall\mathbf{x}} \mathbf{N}(\mathbf{x}, \mathbf{x}+\Delta\mathbf{x})\rho(\mathbf{x}, \mathbf{x}+\Delta\mathbf{x})}{\sum_{\forall\mathbf{x}} \mathbf{N}(\mathbf{x}, \mathbf{x}+\Delta\mathbf{x})} = \begin{bmatrix} \bar{\rho}_{uu} & \bar{\rho}_{uv} \\ \bar{\rho}_{vu} & \bar{\rho}_{vv} \end{bmatrix}. \qquad (16)$$

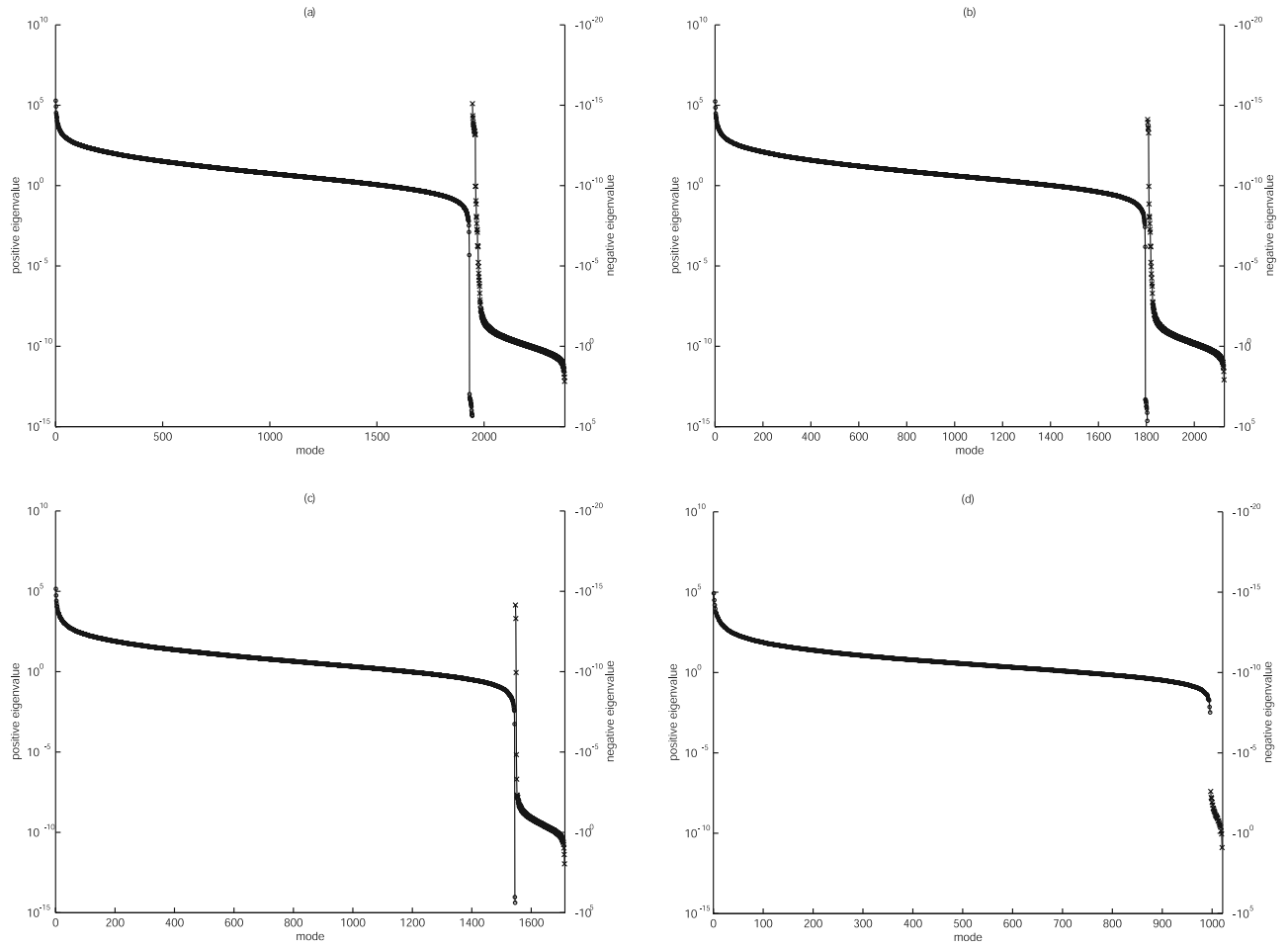

Figure 10. The eigenvalue spectrum of the sample data covariance matrix with varying data coverage. The positive and negative eigenvalues are indicated with circles and crosses, respectively. (a) 1188 grid points (60% coverage), (b) 1062 grid points (70% coverage), (c) 856 grid points (80% coverage), and (d) 510 grid points (90% coverage).

The sample mean standard deviations, $\bar{\sigma}(\mathbf{x})$, can be smoothed by fitting to a surface such as a plane

$$\bar{\sigma}(\mathbf{x}) = \begin{bmatrix} \bar{\sigma}_u(\mathbf{x}) \\ \bar{\sigma}_v(\mathbf{x}) \end{bmatrix} = \begin{bmatrix} a_1 x + b_1 y + c_1 \\ a_2 x + b_2 y + c_2 \end{bmatrix}, \tag{17}$$

or by using a constant, which is chosen as the median of the standard deviations in the observation domain.

[30] The smoothed data covariance matrix, $\bar{C}$ ($\mathbf{x}$, $\mathbf{x}'$), is

$$\bar{\mathbf{C}}(\mathbf{x}, \mathbf{x}') = \bar{\rho}(\Delta\mathbf{x})\bar{\sigma}(\mathbf{x})\bar{\sigma}(\mathbf{x}'). \tag{18}$$

4. Results

4.1. Decorrelation Length Scale

[31] The decorrelation length scale provides a basis for the physical interpretation of surface currents. The locally averaged correlation coefficients (equation (11)) of the eastward currents (or northward currents) are fit with an exponential function (equation (12)) as above, and the decay scales of the exponential function are represented by the semimajor and semiminor axes as well as by the rotation of ellipses.

[32] In order to examine the variability of surface currents across the coast, we focus on the grid points along a line of constant latitude shown as line A in Figure 1. The locally averaged correlation coefficients of eastward currents (or northward currents) at grid points ($\hat{\mathbf{x}}$) within 4 km radius (r_0) from the reference grid points ($\mathbf{x}$) are fit with an exponential function. The maximum lag, $n = 3$, was chosen as the low end of a band of lags ($n = 2, 3, \ldots, 8$) from the residuals in equation (13), which all give similar decorrelation length scale estimates within 10–15%. The ellipses of eastward currents (Figure 9a (i)) and northward currents (Figure 9a (ii)) are shown, and the polarization of the axes is nearly constant along line A. The decorrelation length scale of east-west flow (u) decreases from offshore to the coast in the x and y directions, at least partly due to the effects of decreasing depth and the boundary layer of of coastline as shown in Figure 9b. Dominant southeastward currents in the south of San Diego are parallel to the shoreline, resulting in a long decorrelation length scales in the north-south flow (v).

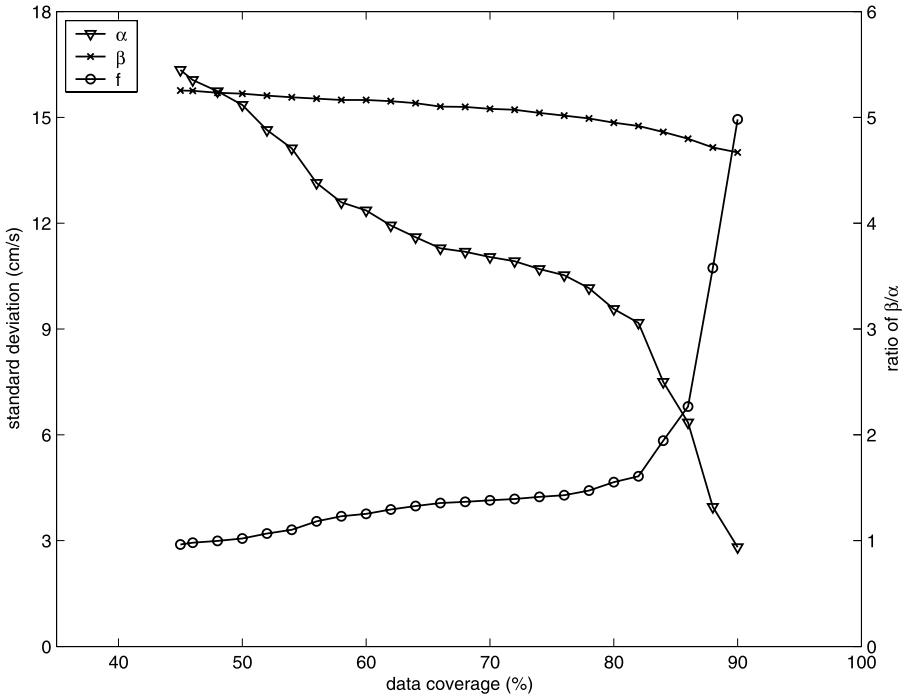

Figure 11. Triangles indicate the square root of the magnitude of the most negative eigenvalue of the sample data covariance matrix as a function of data coverage (α). Crosses are the square root of the average variance of the surface current magnitudes at all grid points with the indicated data coverage (β). Circles are the ratio ($f = \beta/\alpha$).

Peaks at 13 km offshore in the x direction and at 18 km offshore in the y direction are shown.

4.2. Uncertainty

[33] The number and magnitude of negative eigenvalues of the sample data covariance matrix depend on how many data are missing in the data set used for the estimation of the covariance matrix. Figure 10 shows the eigenvalue spectrum for several threshold values of the data coverage (60, 70, 80, and 90%). As the estimate was restricted to regions of increasing coverage, the number of negative eigenvalues decrease as do their magnitudes. If the data were 100% present there would be no negative eigenvalues. The most negative eigenvalue is a measure of the error in the sample data covariance compared to the true covariance matrix which must be non-negative definite. In order to make the covariance matrix non-singular a diagonal covariance matrix with uniform variance (γ^2) is added to the sample data covariance matrix. This must be large enough to compensate for the worst negative eigenvalue to restore the positive definite condition for the matrix inversion as discussed above. In standard objective mapping, where the covariance matrices are assumed to be known in advance and are positive definite, the regularization matrix (**R**) controls the amount of filtering in the mapping. This regularization is an artificial addition to remove the negative eigenvalues in this application. This is not an elegant method compared to other methods, but is simple and allows some representative calculations.

[34] The uncertainty of the objectively mapped current vectors differs from the geometric dilution of precision (GDOP). We assumed all data are equally good regardless of GDOP, and the mapping error is determined by data coverage alone. The uncertainty presented here represents the expected uncertainty in the map due to missing data and measurement errors. The square root of the absolute value of the most negative eigenvalue of the sample data covariance matrix as a function of data coverage (α, triangle), the square root of the averaged variance of the surface current magnitudes at all grid points with the indicated data coverage (β, cross), and their ratio ($f = \beta/\alpha$, circle) are shown in Figure 11.

[35] The sample data covariance matrix with 90% coverage has a most negative eigenvalue of -7.9 (cm/s)^2. In the objective mapping with this covariance matrix, a regularization matrix is added as a diagonal matrix with 10% of the averaged variance of sample covariance matrix (γ = 4.42 cm/s), which is larger than the square root of the magnitude of the most negative eigenvalue. This γ is chosen arbitrarily as a "reasonable" value, which leads to the estimation of surface currents with about 4 cm/s uncertainty. Qualitatively similar results are obtained for γ^2 in the range of 5–15% of the averaged variance of the sample covariance matrix.

4.3. Smoothed (Homogeneous) Covariance Matrix

[36] The contour plots of the sample mean correlation coefficients (equation (16)) between eastward currents and northward currents present the exponential structure as shown in Figures 12a and 12b, respectively. The mean correlation coefficients are constructed in order to exclude spurious small-scale structures due to missing data and to

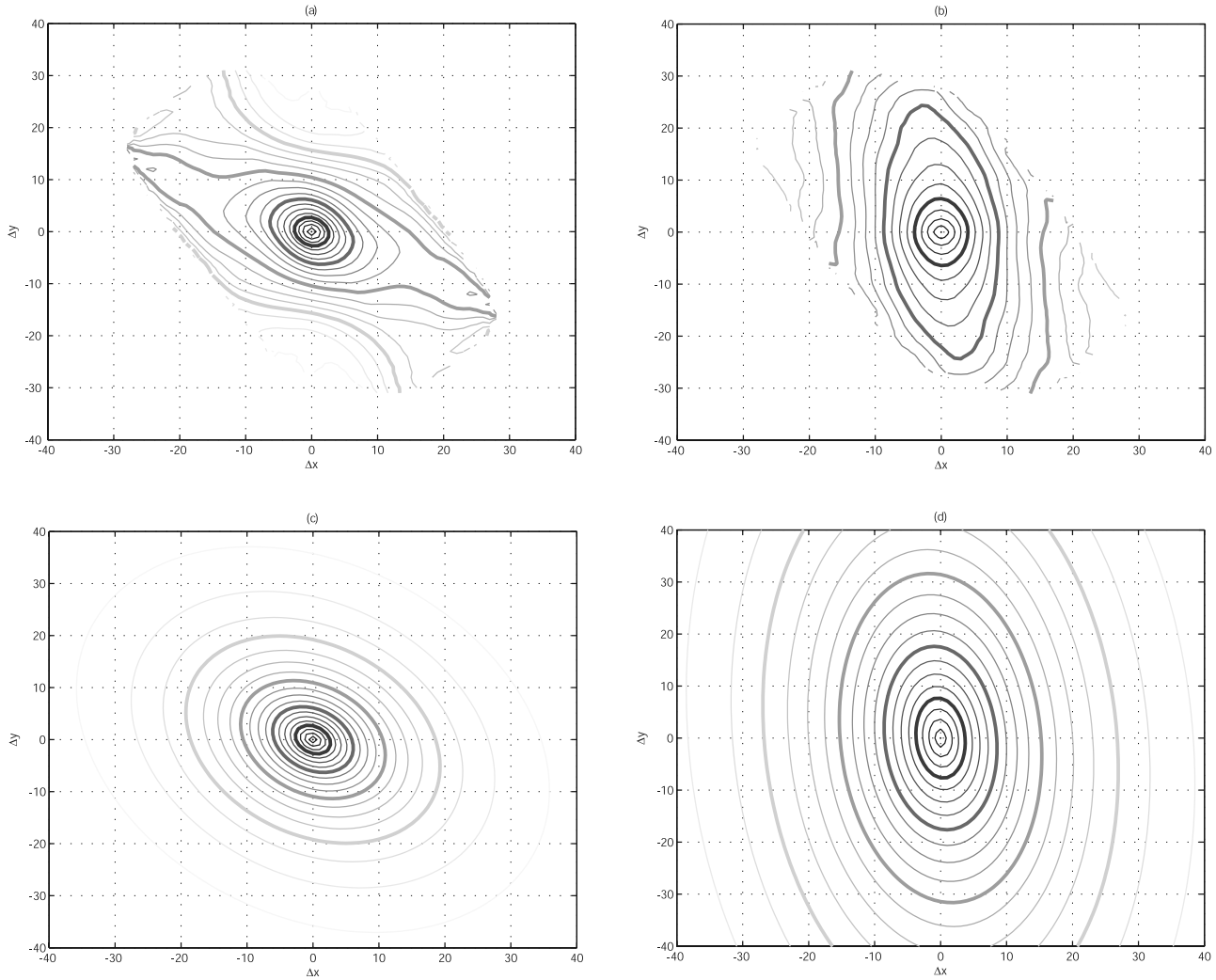

Figure 12. The spatially averaged correlation coefficients (equation (16)) between (a) eastward currents, $\bar{\rho}_{uu}(\Delta x, \Delta y)$, and (b) northward currents, $\bar{\rho}_{vv}(\Delta x, \Delta y)$. Exponential functions (equation (12)) fitted to the spatially averaged correlation coefficients between (c) eastward currents and (d) northward currents. The spacing of thin contours is 0.05, and thick contours are at 0.2, 0.4, 0.6, and 0.8.

achieve a more robust estimate of the covariance matrix by horizontal averaging. The mean of the cross correlation term between eastward (u) and northward (v) currents shows nearly flat structure varying within ±0.2. Therefore, the cross term of correlation for the smoothed covariance matrix is set to zero.

[37] The mean correlation coefficients within $\pm 20\Delta x$ and $\pm 20\Delta y$ from the center are fitted with an exponential function (equation (12), $n = 20$). Since the mean correlation is smoother than the locally averaged correlation (equation (11)), it is fitted with larger n and results in smaller residual variance. The contour plots of smoothed correlation coefficients are shown in Figures 12c and 12d. The fitting coefficients and decorrelation length scales are shown in Tables 1a and 1b, respectively. The coefficients (a, b, and c) are a function of the spatial lag (Δx, Δy), getting flatter away from the center. However, for simplicity in calculations we assumed these coefficients as constant.

[38] The standard deviation of surface currents might be assumed to depend on the bottom bathymetry in shallow water or the distance from the coastline (Figure 4b).

Table 1a. Coefficients (a, b, and c) of the Exponential Function Fitted to the Spatially Averaged Correlation Coefficients (Equation (12))

	a	b	c
$\bar{\rho}_{uu}(\Delta x, \Delta y)$	0.0075	0.0038	0.007
$\bar{\rho}_{vv}(\Delta x, \Delta y)$	0.0036	0.0004	0.009

Table 1b. Decorrelation Length Scales (km) of the Eastward Current (u) and the Northward Current (v) in the x and y Directions

	x-Direction	y-Direction
u	13.7	10.4
v	16.6	34.6

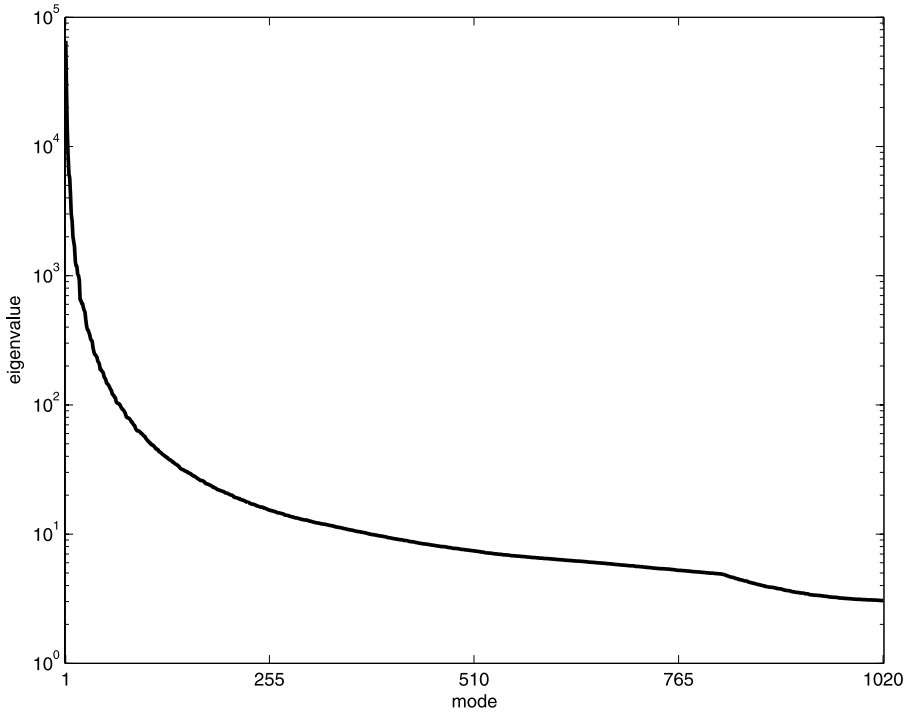

Figure 13. The eigenvalue spectrum of the smoothed data covariance matrix.

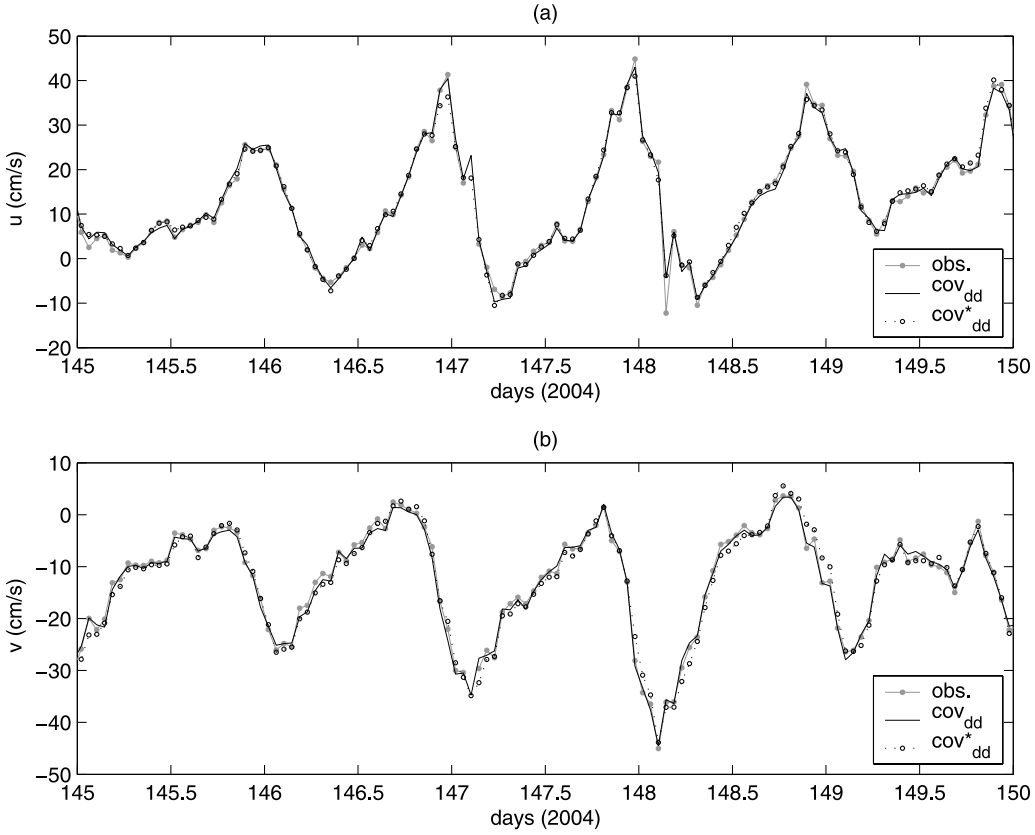

Figure 14. The sample time series: the raw data (gray dots), the objectively mapped data using the sample data covariance matrix (black line), and the objectively mapped data using the smoothed data covariance matrix (black dotted).

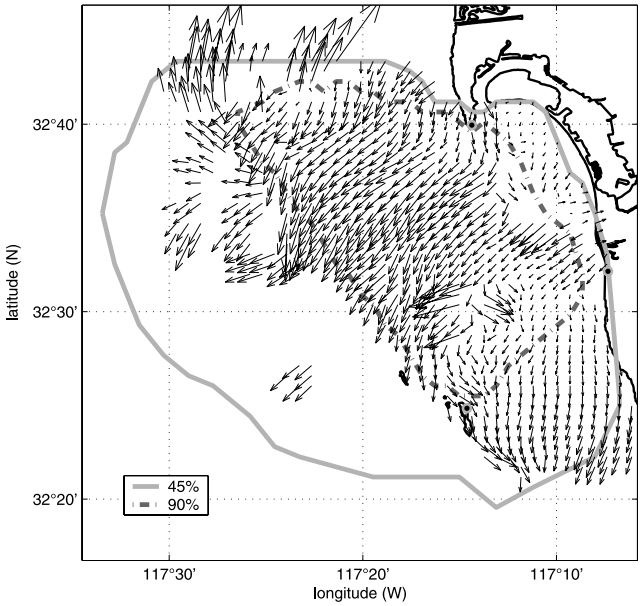

Figure 15. An example of the current vector field. The data coverage is indicated with contours.

Accordingly, the smoothed standard deviation of surface currents might be fitted by spatial functions such as bathymetry or distance from the coastline. However, since some standard deviations near baselines are high and are inconsistent with the nearby area, it could be difficult to avoid the influence of spurious data. Therefore, the smoothed standard deviation of eastward currents (or northward currents) is estimated from the median value of standard deviations at all observation grid points. The median value for eastward currents, $\bar{\sigma}_u(x, y)$, and northward currents, $\bar{\sigma}_v(x, y)$, are 12.21 and 16.41 cm/s, respectively.

[39] The smoothed covariance matrix of surface currents is reconstructed by multiplying the spatial mean correlation coefficients (equation (16)) at the spatial lag (Δx, Δy) and the smoothed standard deviations at all grid points (x, y). The eigenvalue spectrum of the smoothed covariance matrix is shown in Figure 13. The smallest eigenvalue of the smoothed covariance matrix is 3.91 $(\text{cm/s})^2$, and a diagonal matrix with 10% of averaged variance is added as the regularization matrix (γ = 4.57 cm/s). The smoothed covariance matrix is positive definite, and the regularization has a reasonable noise level as discussed above.

4.4. Comparison of Gridding

[40] The surface current vectors measured at 510 grid points (90% coverage) for one month were mapped objectively with both the sample data covariance matrix of two year span and the smoothed data covariance matrix. The data covariance matrix can only map in the 90% coverage area, while the smoothed covariance matrix can be used for the expanded 45% coverage area.

4.4.1. Time Domain

[41] The observed and the objectively mapped eastward currents (u) and northward currents (v) are shown in Figures 14a and 14b. As a random example having missing data, these time series are at a grid point within the 90% coverage area. The estimated data with both covariance matrices agree with the observations, and suppress the spurious data. Since the estimated data usually have less variance than the observations due to the regularization, a variance or covariance estimated from the objectively mapped surface currents will be biased.

4.4.2. Space Domain

[42] An example of the surface current vector field is shown with the 90% (dashed contour) and 45% (gray contour) coverage area in Figure 15. Spurious data can be seen on the baselines (SDPL and SDBP, SDPL and SDCI) and at the edge of the observation domain (at the west of Point Loma). Moreover, there are missing data on the baselines and at the west of the Coronado Islands.

[43] The objectively mapped current vector field on grid points in the 90% and 45% coverage area is shown in Figures 16a and 16b, respectively. The spurious data are suppressed, and the gaps in space are filled with a consistent current vector field. The current vector field mapped with the smoothed data covariance matrix shows a smoother field.

[44] The objectively mapped uncertainty field for two coverage cases are shown in Figures 16c and 16d. The uncertainties normalized by the variance of the surface current at each grid point vary from 0 (more reliable) to 1 (more uncertain), and are represented as ellipses to include directional information. However, since the smoothed covariance matrix assumed no cross correlation between the eastward current (u) and the northward current (v), the ellipses are not tilted in Figure 16d. Higher uncertainty occurs in the baseline of SDPL and SDBP (Figure 16c) and the area with fewer radial velocities (Figure 16d).

5. Discussions and Conclusions

[45] There are a number of ways to map gappy observations to a complete grid. Some methods use prior estimates of covariance functions either from analytical functions or from basis functions (or ''normal modes'') determined from models. The approach we have described involves the use of the observed covariance matrix in objective mapping and the challenges faced when dealing with the negative eigenvalues of the sample covariance matrix.

[46] There are several assumptions used in the objective mapping technique described in this paper. First, the mean of the observations is assumed to be the same as the mean of the estimated data. Since the grid points where the current vectors are estimated are the same as where the current vectors are observed, this assumption is valid under the circumstances when there are sufficient number of unbiased observations to estimate mean currents. Second, since the fraction of missing observations is closely related to the size of the negative eigenvalues, there is a restriction in the estimation of the surface current vectors with reasonable uncertainty through the objective mapping using the sample data covariance matrix. Finally, the cross correlations ($\bar{\rho}_{uv}$), between the eastward current (u) and the northward current (v) are assumed zero in the smoothed data covariance matrix. The decorrelation length scales and standard deviations are assumed as constant in the observation area. However, the smoothed covariance matrix might be improved by using locally averaged decorrelation length scales and standard deviations related to the bottom bathymetry.

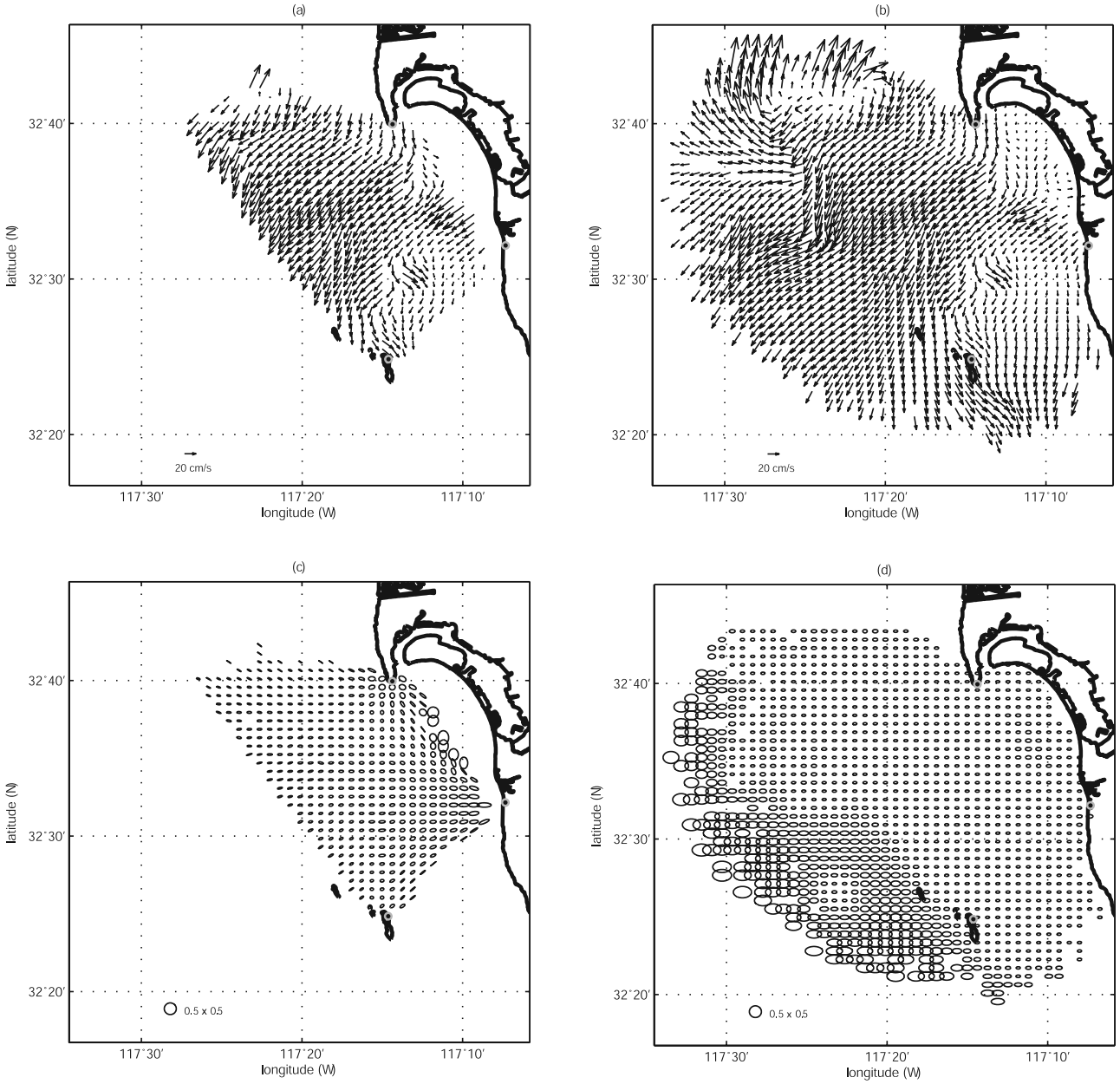

Figure 16. An example of the objectively mapped current vector field using (a) the data covariance matrix in the region with 90% data coverage and (b) the smoothed covariance matrix in the region with 45% data coverage. (c) and (d) Normalized uncertainty ellipses corresponding to Figures 16a and 16b.

[47] The objective mapping of surface currents enables us to get complete current vector fields for real time applications. The integration in time and the differentiation in space of surface currents are applicable to particle tracking for pollutants, rescue, and dispersion of larvae, and estimates of divergence and vorticity (e.g., upwelling and downwelling). As an ongoing application, the Tijuana River plume has been tracked with a random walk model based on the objectively mapped surface currents. The decorrelation length scales and the correlation functions estimated from the observed surface currents provide the initial steps for the statistical surface current models. In order to build this model, the data covariance matrix should have enough realizations to include the response of surface currents to the various driving forces.

[48] This job work was carried out in MATLAB on a dual Xenon CPU (4G RAM) machine running Linux. The hourly gridding for 1337 grid points takes about 20–30 seconds. The dominant computation is from the inversion of the covariance matrix.

[49] **Acknowledgments.** We would like to acknowledge the generous sponsors of this work. Sung Yong Kim is supported through a graduate student fellowship provided by the California Institute of Telecommunication and Information Technology (CALIT2). Eric Terrill is supported through funding provided by the Office of Naval Research (ONR), NOAA, and the State of California. The observing system infrastructure used in this research was supported by the California Clean Beaches Initiative and its

continued operation is provided by both the State of California under the Coastal Ocean Currents Monitoring Program (COCMP), and through NOAA under a grant to develop the Southern California Coastal Ocean Observing System (SCCOOS). Bruce Cornuelle is supported by both NOAA and COCMP.

References

Alvera-Azcarate, A., A. Barth, M. Rixen, and J. Beckers (2005), Reconstruction of incomplete oceanographic data sets using empirical orthogonal functions: Application to the Adriatic Sea surface temperature, *Ocean Modell.*, *9*, 325–346.

Beckenbach, E., and L. Washburn (2004), Low frequency waves in the Santa Barbara Channel observed by high frequency radar, *J. Geophys. Res.*, *109*, C02010, doi:10.1029/2003JC001999.

Beckers, J. M., and M. Rixen (2003), EOF calculations and data filling from incomplete oceanographic datasets, *J. Atmos. Oceanic Technol.*, *20*, 1839–1856.

Boyd, J. D., E. P. Kennelly, and P. Pistek (1994), Estimation of EOF expansion coefficients from incomplete data, *Deep Sea Res., Part I*, *41*(10), 1479–1488.

Brankart, J. M., and P. Brasseur (1996), Optimal analysis of in situ data in the western Mediterranean using statistics and cross-validation, *J. Atmos. Oceanic Technol.*, *13*, 477–491.

Bretherton, F. P., R. E. Davis, and C. B. Fandry (1976), A technique for objective analysis and design of oceanographic experiment applied to MODE-73, *Deep Sea Res.*, *23*, 559–582.

Chapman, R. D., L. K. Shay, H. Graber, J. B. Edson, A. Karachintsev, C. L. Trump, and D. B. Ross (1997), On the accuracy of HF radar surface current mesurements: Intercomparisons with ship-based sensors, *J. Geophys. Res.*, *102*(C8), 18,737–18,748.

Davis, R. E. (1985), Objective mapping by least squares fitting, *J. Geophys. Res.*, *90*(C7), 4773–4778.

Denman, K. L., and H. J. Freeland (1985), Correlation scales, objective mapping and a statistical test of geostrophy over the continental shelf, *J. Mar. Res.*, *43*, 517–539.

de Paolo, T., and E. Terrill (2007), Skill assessment of resolving ocean surface current structure using Compact-Antenna style HF RADAR and the MUSIC direction finding algorithm, *J. Atmos. Oceanic Technol*, in press.

Essen, H.-H., K.-W. Gurgel, and F. Schirmer (1983), Tidal and wind-driven parts of surface currents as measured by radar, *Dt. Hydrogr. Z.*, *36*(3), 81–96.

Graber, H. C., B. K. Haus, R. D. Chapman, and L. K. Shay (1997), HF radar comparisons with moored estimates of current speed and direction: Expected differences and implications, *J. Geophys. Res.*, *102*(C8), 18,749–18,766.

Gurgel, K.-W. (1994), Shipborne measurements of surface current fields by HF radar, *L'Onde Electr.*, *74*(5).

Hollingsworth, A., and P. Lönnberg (1986), The statistical structure of short-range forecast errors as determined from radiosonde data. Part I: The wind field, *Tellus, Ser. A*, *38*, 111–136.

Houseago-Stokes, R. E., and P. G. Challenor (2004), Using PPCA to estimate EOFs in the presence of missing values, *J. Atmos. Oceanic Technol.*, *21*, 1471–1480.

Levanon, N. (2000), Lowest GDOP in 2-D scenarios, in *IEE Proceeding*, pp. 149–155, IEE Proc. Radar, Sonar Navig., London.

Lipa, B. J., and D. E. Barrick (1983), Least squares methods for the extraction of surface currents from CODAR crossed-loop data: Application at ARSLOE, *IEEE J. Oceanic Eng.*, *13*(2), 507–513.

Lipphardt, B. L., Jr., A. D. Kirwan Jr., C. E. Grosch, J. K. Lewis, and J. D. Paduan (2000), Blending HF radar and model velocities in Monterey Bay through normal mode analysis, *J. Geophys. Res.*, *105*(C2), 3425–3450.

Munk, W. H., and D. E. Cartwright (1966), Tidal spectroscopy and prediction, *Philos Trans., Ser. A, Phys. Eng. Sci.*, *259*(1105), 533–581.

Orchard, T., and M. A. Woodbury (1972), A missing information principle: Theory and applications, in *Proceedings of the 6th Berkeley Symposium on Mathematics, Statistics, and Probability*, Univ. of Calif. Press, Berkeley.

Schneider, T. (2001), Analysis of incomplete climate data: Estimation of mean values and covariance matrices and imputation of missing values, *J. Clim.*, *14*, 853–871.

B. Cornuelle, Physical Oceanography Research Division, Scripps Institution of Oceanography, 9500 Gilman Dr., La Jolla, CA 92093, USA. (bdc@ucsd.edu)

S. Y. Kim and E. Terrill, Marine Physical Laboratory, Scripps Institution of Oceanography, 9500 Gilman Dr., La Jolla, CA 92093, USA. (syongkim@mpl.ucsd.edu; eterrill@ucsd.edu)